Small polaron formation on the Nb-doped SrTiO$_3$(001) surface

Florian Ellinger [1], Muhammad Shafiq [2], Iftikhar Ahmad [3,4], Michele Reticcioli [1], and Cesare Franchini [1,5]

[1]*Center for Computational Materials Science, Faculty of Physics, University of Vienna, 1090 Vienna, Austria*

[2]*Department of Physics, Abbottabad University of Science and Technology, Abbottabad 22020, Pakistan*

[3]*Department of Physics, University of Malakand, Chakdara 18800, Khyber-Pakhtunkhwa, Pakistan*

[4]*Center for Computational Materials Science, University of Malakand, Chakdara 18800, Khyber-Pakhtunkhwa, Pakistan*

[5]*Dipartimento di Fisica e Astronomia, Università di Bologna, 40127 Bologna, Italy*

The cubic perovskite strontium titanate SrTiO$_3$ (STO) is one of the most studied, polarizable transition metal oxides. When excess charge is introduced into this material through doping or atomic defects, STO tends to host polarons: quasiparticles formed by excess charge carriers coupled to the crystal phonon field. Their presence alters the properties of this material and is a key for many applications. Considering that polarons form preferentially on or near surfaces, we study small polaron formation at the TiO$_2$ termination of the STO(001) surface via density functional theory calculations. We model several supercell slabs of Nb-doped and undoped STO(001) surfaces with increasing size, also considering the recently observed as-cleaved TiO$_2$-terminated surface hosting Sr adatoms. Our findings suggest that small surface polarons become less stable at low concentrations of Nb doping, in analogy to polarons localized in the bulk. Further, we inspect the stability of different polaron configurations with respect to Nb and Sr impurities and discuss their spectroscopic properties.

I. INTRODUCTION

Transition metal oxide perovskites are an incredibly versatile and intriguing class of materials with electronic properties which are relevant for a wide range of applications. In particular, SrTiO$_3$ (STO) exhibits many properties arising on its surface and at the interface with other materials, including the emergence of a two-dimensional electron gas (2DEG) [1–3], that are potentially useful for technological applications in the field of photoemission [4], (photo)catalysis [5–8] and superconductivity [9]. Nowadays, STO is one of the most investigated perovskite materials because it is a promising candidate in oxide electronics.

The STO(001) surface has attracted a lot of attention in recent experiments [10,11]. Both the 1×1 unreconstructed TiO$_2$ and SrO terminations show a weakly polar character and exhibit surface rumpling, together with a small dipole moment [12–14]. During cleaving, the STO(001) surface imposes challenges to sample preparation, leading to inconsistent and partially contradicting data in the literature [15]. Just recently, a low-temperature, unreconstructed termination of the STO(001) surface with 1×1 symmetry via cleaving was obtained [16]. The authors were able to introduce a preferential cleavage plane by putting *n*-type (Nb-)doped STO crystals under strain. Their scanning probe microscopy measurements on the as-cleaved surface show well-defined, large TiO$_2$- and SrO-terminated terraces, with a canonical amount of $14\% \pm 2\%$ Sr adatoms and Sr vacancies, respectively [17]. The spontaneous formation of these defects during the cleaving process was interpreted as a mechanism for polarity compensation.

Intrinsic Sr adatoms and Sr vacancies influence the electronic properties of the surface by introducing excess charge carriers into the system. Similar to charge carriers introduced by doping (e.g., substituting Ti by Nb), extra charge from the Sr defects can couple to the crystal phonon field by inducing local distortions in the lattice. As a consequence, these distortions can create a potential well for the charge to localize in a certain region of the crystal, forming a polaron quasiparticle [18,19]. Polarons have grown to be a major topic of interest in the field of semiconducting and insulating materials, particularly in oxides. Recent studies revealed that these self-trapped charge carriers influence a wide spectrum of physical and chemical properties of the host material [20–22]. In STO polarons have been reported to affect charge transport [23], dielectric properties [24], and emission spectra [25].

Depending on the crystal, charge coupling to lattice distortions and subsequent self-trapping can occur over different length scales: While small polarons are formed by short-range coupling and are usually confined within one unit cell, large polarons spread over many unit cell lengths and are formed in the long-range coupling regime. As a particularly interesting behavior, STO not only shows stable electron polarons but can also exhibit delocalized charge in the bulk crystal [26,27], defect states [28], and a 2DEG on surfaces [1,2]. This multitude of observed electronic states could hint at localized charge in the form of small polarons coexisting with delocalized charge and/or large polarons (e.g., depending on the charge carrier doping).

Despite Nb being a natural impurity in STO and its technical relevance in experiments [29,30], theoretical studies investigating Nb doping in STO crystals are scarce. Hao *et al.* investigated small polaron formation in Nb-doped STO bulk systems, finding a trend towards polaron destabilization in doping sparse environments [26]. Eglitis explored the influence of Nb doping on the structural and electronic environment in its surroundings in the STO crystal [31] but did not consider polaron formation.

TABLE I. Difference in total energy for Nb doping placed in different layers of the slab. Calculations were done for a $2\sqrt{2} \times 2\sqrt{2} \times 6$ slab and a delocalized excess electron.

Layer	S0	S1	S2	S3
ΔE (meV)	+3	0	+61	+63

Many theoretical studies facilitating excess charge consider oxygen vacancies V_O to be electron-donating defects, although they generally do not report small polaron formation in STO. Defect states in the form of charged V_O were found using density functional theory (DFT+U+V) methodology [32], and excess electrons forming charged V_O defect states or delocalized solutions occupying the conduction band were reported previously [33]. The influence of doping (other than Nb) on the carrier lifetime of the defect state associated with V_O was also investigated recently [34].

Existing literature discussing polaron formation in STO mostly investigated large polarons, where the experimental optical response of n-doped STO was reproduced by using a large polaron picture [35,36], and large polaron formalism was facilitated to study the transition from a polaronic liquid to a Fermi liquid regime with increasing doping concentration in STO [37]. Other studies did not find evidence for small polaron formation in STO at all [38].

The Sr adatom and Sr vacancy surface defects are even less studied than Nb-doped STO, with no theoretical work done up to this point to our knowledge.

The technical relevance of polarons, together with the recent experimental description of a well-defined, as-cleaved surface motivates a reexploration of the low-temperature, ground-state STO(001) surface by first-principles calculations to account for Nb doping, as well as surface defects, at variance with earlier theoretical studies.

To address this gap in the literature, we perform a DFT study investigating polaronic properties of the TiO$_2$-terminated STO(001) surface. The aim of this study can be divided into two main parts: (1) the investigation of small electron polarons on the surface, introduced into the n-type doped STO crystal by Nb atomic substitution, and (2) the analysis of

polaronic properties of the as-cleaved, low-temperature experimental surface including Sr adatoms, as recently described in Refs. [16,17]. We consider (self-)trapped small electron polarons throughout the study; however, for simplicity we refer to them simply as polarons from now on.

In the first part, a working setup for polaron localization in STO is deducted. Using this setup, polaron formation energies are then calculated for different Nb-doping concentrations. Afterwards, results from the first part will be used for modeling and investigating the as-cleaved TiO$_2$ termination, including Sr adatoms. We compare different polaron configurations and generate simulated scanning tunneling microscopy (SSTM) images for different environments.

II. METHODS

A. Computational setup

Calculations were done using the Vienna *Ab initio* Simulation Package (VASP) [39–41]. Projector augmented-wave Perdew-Burke-Ernzerhof potentials were used [42–44]. Since charge localization is spuriously disfavored in standard DFT, we employed an on-site energy correction term within the DFT+U framework to describe small polaron localization. For this, we chose the rotationally invariant implementation, as introduced by Dudarev *et al.* [45], with a value of $U - J = 4.5$ eV, enacted on the d orbitals of Ti and Nb atoms. This is consistent with the choice of U in earlier works using values calculated by constrained random phase approximation [26,46,47].

B. Supercells

To model both the bulklike and as-cleaved, low-temperature TiO$_2$ terminations of the STO(001) surface, we used asymmetric slabs with a thickness of six unit cell layers. Each unit cell layer consists of one TiO$_2$ and one SrO monolayer, amounting to 12 stacked monolayers in total. We adopted the low-temperature, antiferrodistortive (AFD) phase of STO, consisting of 20 atoms in the bulk primitive cell, together with experimental lattice parameters ($a = b = 5.5202$ Å, $c = 7.8067$ Å [48]). The bottom two unit cell layers were fixed at the AFD bulk structure, while the atom positions
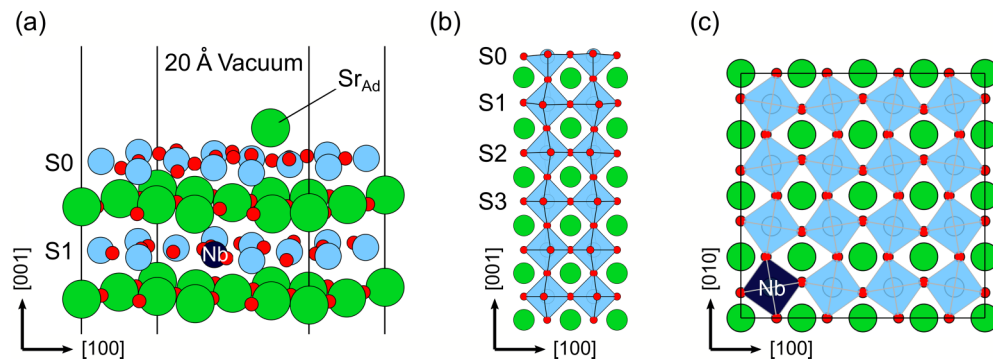

FIG. 1. (a) Schematic representation of the first two layers of the asymmetric STO(001) surface slab. Nb doping is placed in the subsurface (S1) layer, and the Sr adatom is placed at an Sr lattice position on top of the surface. (b) Cross section of a surface slab showing the six unit cell layers (six TiO$_2$ and six SrO monolayers, respectively). The O octahedra around Ti sites are rotated in an alternating manner and are slightly tilted due to the antiferrodistortive (AFD) lattice. (c) Top view of the S1 layer of the 4×4 supercell. One Ti atom is replaced by Nb for doped systems; O octahedra are rotated in an alternating manner due to the AFD distortions.

of the top four layers were relaxed until the norm of all forces was below 0.01 eV/Å. For the ionic relaxation a plane-wave energy cutoff of 550 eV was used, together with a $5 \times 5 \times 1$ k-point grid. The energy cutoff was increased to 700 eV for the final electronic ground-state calculations. Due to STO(001) being a weakly polar surface, a dipole correction along the [001] direction (normal to the surface) was applied [49,50].

Supercells of increasing lateral size were constructed to model the bulklike 1×1 TiO$_2$ termination. For this, the in-plane dimensions of the slab were scaled by a factor of $N = \{2, 2\sqrt{2}, 4, 3\sqrt{2}, 4\sqrt{2}\}$, corresponding to a total number of 1×1 unit cells $N_{\text{unitcell}} = N \times N$. This results in cells ranging from 240 atoms for the smallest ($N \times N = 2 \times 2$) to 960 atoms for the largest one ($4\sqrt{2} \times 4\sqrt{2}$).

The Nb doping was included by substituting one sub-surface (S1) Ti atom, leading to one excess electron in the supercells. The Nb substitution in other layers (in the absence of charge localization) is less stable, as shown in Table I for the $2\sqrt{2} \times 2\sqrt{2} \times 6$ slab. To specify the Nb content of each slab, we define the concentration of Nb in two ways during our analysis: (1) To be consistent with previous works we use a definition with respect to the 2D size of the surface cell ($1/N_{\text{unitcell}}$), and (2) to achieve better comparison with experiments we also indicate the Nb concentration as a percentage with respect to the total number of Ti sites in the slab ($c_{\text{Nb}} = 1$ Nb atom/total number of Ti atoms).

The as-cleaved surface was modeled by adding one Sr adatom to both a pristine slab and a Nb-doped $2\sqrt{2} \times 2\sqrt{2} \times 6$ slab, corresponding to an adatom coverage of 12.5%, closely resembling the experimentally observed coverage of 14% $\pm$ 2% [17]. For the Nb-doped slab, the Sr adatom was placed at the maximally allowed distance between the two defects, as this configuration was found to be the energetically most stable (see the Supplemental Material [51] for details). A schematic view of the adopted slabs is shown in Fig. 1.

C. Polaron localization

The Nb doping and Sr adatoms introduce one and two excess charge carriers, respectively, which can localize in the form of polarons. The polaron stability can be inspected by calculating the polaron formation energy E_{pol}, defined as the difference between the total energy of the system containing localized polarons ($E_{\text{loc}}^{\text{tot}}$) and the system with excess charge being delocalized ($E_{\text{deloc}}^{\text{tot}}$):

$$E_{\text{pol}} = E_{\text{loc}}^{\text{tot}} - E_{\text{deloc}}^{\text{tot}}. \quad (1)$$

Therefore, a stable polaron is characterized by a negative formation energy, while a positive energy reflects a tendency towards delocalization.

Different localization sites and polaronic arrangements were inspected. Two different approaches were adopted to induce localization of the small electron polarons at the desired Ti site: (1) The first is a stepwise procedure, in which distortions around the localization site are induced by intermediate replacement of the Ti atom with V. After resubstitution, the polaron forms at the selected site [52]. (2) The second approach is charge localization using an occupation matrix control tool (OCCMATRIX) [53], in which orbital occupations are initialized directly through a hard constraint in a prelimi-
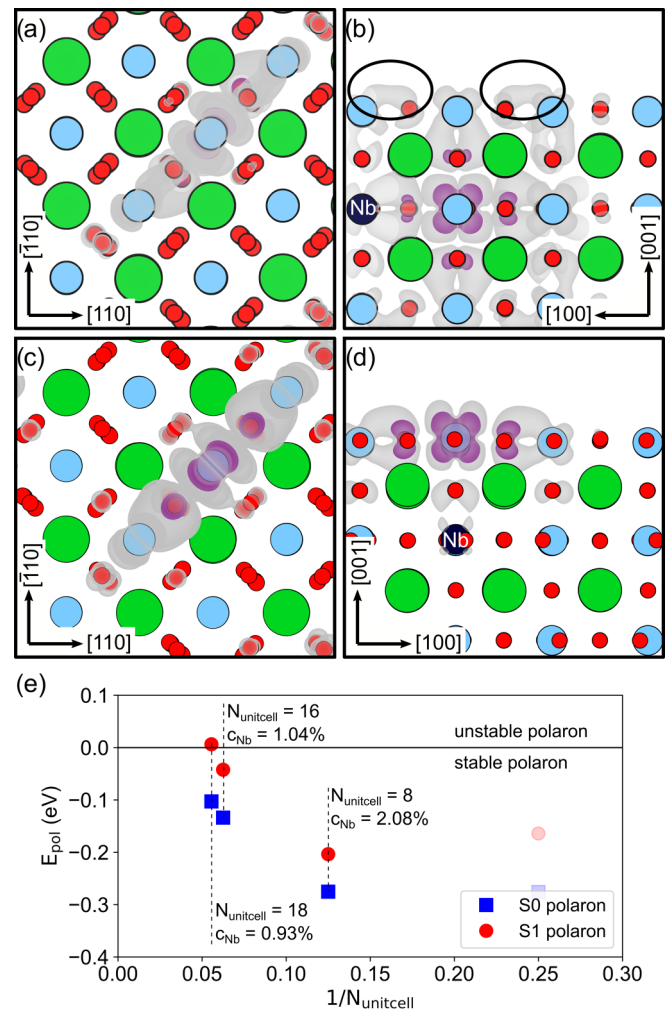

FIG. 2. Charge isosurface of single polarons and corresponding formation energies E_{pol} for different supercell sizes. (a) Top and (b) side views of the S1 polaron, localized at a Ti site next to Nb. Polaronic charge localized at Ti-O bonds (encircled) creates the strongest signal in SSTM images discussed in Sec. III C. (c) Top and (d) side views of a S0 polaron, localized at a Ti site on the surface, directly above Nb. (e) Polaron formation energies as a function of Nb-doping concentration for S0 and S1 polarons. Surface polarons (S0) are more stable than polarons localized in the S1 layer, where for the latter charge delocalization is favored for the $3\sqrt{2} \times 3\sqrt{2} \times 6$ supercell already. The 2×2 supercells (light shaded points) are excluded from further analysis, as for these systems the DOS and isosurfaces suggest polaron self-interaction due to finite-size effects (see [51]).

nary calculation. In this way, polaronic charge can be placed in the desired Ti orbital explicitly, and distortions are induced by the excess charge directly.

The polaron solutions obtained using either procedure are independent of the specific localization method. In both cases, a final, full ionic relaxation is performed to let the system relax into the preferable, unconstrained energy minimum. We further note that only spin-aligned configurations were considered, as spin ordering does not cause a sizable change in total energies or charge density distributions (see [51]). This

means that all polarons are localized within the same spin channel in our spin-polarized calculations. The OCCMATRIX approach was used for most results; only the formation energies for S1 polarons shown in Fig. 2(e) were calculated using the stepwise procedure.

The advantages of the OCCMATRIX approach are a faster and more straightforward protocol and the precise control of the selected trapping site. A downside is that it needs an initial educated guess for the polaron orbital. These orbital configurations can be extracted from previous calculations with an already localized polaron. Since the characteristic octahedral crystal structure is similar for all calculations done here, the preferred orbitals for polaron localization, governed by the crystal field, do not change drastically between supercells. Further, even when starting from a rough initial guess, the excess charge typically has enough freedom to find the lowest-energy solution during the final, unconstrained self-consistent calculation and relaxes into the lowest-energy orbital. This was generally true during our work and also confirmed by the OCCMATRIX developers [53]. However, in some cases, when two solutions are close in energy, the initial orbital guess can lead to different polaronic orbitals. One critical aspect is that the induced distortions need to be large enough for the polaron to localize. In some calculations this required an increase of the polaron orbital occupation in the initial guess, i.e., placing more than one additional electron, to guarantee electron trapping.

SSTM images of the STO(001) surface were obtained by considering the partial charge density of the in-gap polaron states at approximately 3 Å above the surface.

III. RESULTS

A. Polaron stability on the bulklike termination

We calculated polaron stability depending on the doping concentration by localizing one polaron in the Nb-doped slabs with varying lateral size (see Fig. 2). The polaron was localized at a Ti site next to (S1 polaron) or above (S0 polaron) the subsurface Nb dopant. These represent the most favorable localization sites, as obtained in a preliminary search in which we tested all possible Ti sites within the S0 and S1 layers of the $4 \times 4 \times 6$ slab (see Fig. SF1 in [51]). The calculations suggest that the polaron binding energy is largest (more negative) when the polaron is located closer to the Nb impurity, meaning that there is a certain tendency of the trapped electron to be pinned by Nb defects. However, stable polarons can also form in sites farther away from the Nb defect (see Fig. SF1(c) in [51]).

Figures 2(a)–2(d) show the polaronic charge density of these two kinds of polarons. In both cases, the polarons occupy d orbitals of Ti atoms in the t_{2g} symmetry group (d_{xz} and d_{yz} orbitals, preferably). This leads to orbital lobes being aligned with the O octahedron surrounding the polaronic Ti ion [see Figs. 2(a)–2(d)]. We note that it was energetically unfavorable to obtain different solutions, even when making use of the occupation matrix constraints. However, the presence of defects might alter this scenario, as discussed later in Sec. III B for the as-cleaved surface with Sr adatoms.
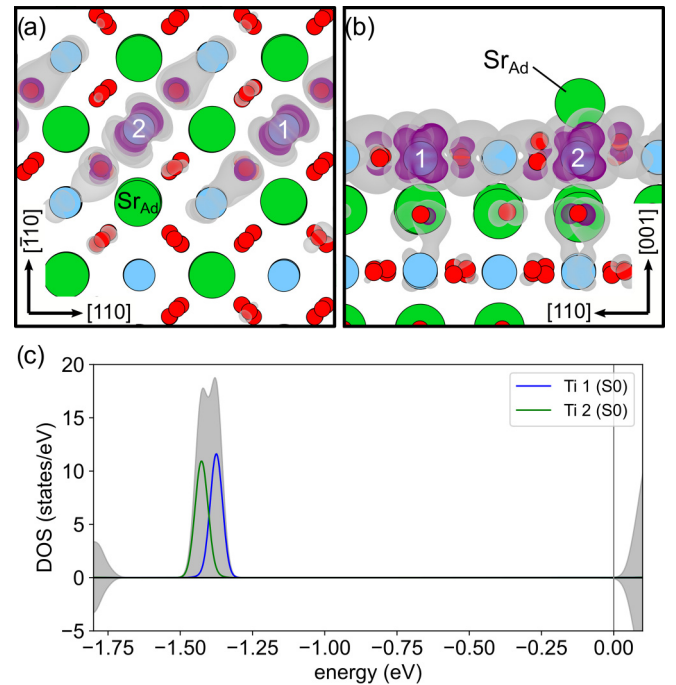

FIG. 3. Polaron charge isosurfaces of the undoped surface slab with a Sr adatom (Sr$_{Ad}$) in (a) top and (b) side views. (c) Corresponding in-gap region of the partial density of states (PDOS) of the two polaronic Ti sites (solid lines), as well as the total DOS (gray shaded area).

The formation energy E_{pol} trend for S0 and S1 polarons as a function of Nb doping is shown in Fig. 2(e). Clearly, at high doping levels (corresponding to a dense polaron population) the formation energy of both the S0 and S1 polarons follows a seemingly linearly decreasing trend for increasing doping concentration within the investigated regime. Conversely, a polaron instability arises at low doping concentrations. For the S1 polaron the crossover to the unstable regime is reached in the $3\sqrt{2} \times 3\sqrt{2} \times 6$ STO(001) supercell, corresponding to a doping concentration of $c_{Nb} = 0.93\%$ (1 Nb and 107 Ti ions). When estimating a similar trend, the crossover for the S0 polaron is estimated to take place at a Nb doping concentration of $c_{Nb} = 0.33\%$. At lower concentration levels, polaron formation becomes highly unfavorable, deviating from the linear trend: For example, the S1 polaron in the larger $4\sqrt{2} \times 4\sqrt{2} \times 6$ surface slab (doping level of $c_{Nb} = 0.52\%$) shows a positive formation energy of $E_{pol} = 2.346$ eV (not shown in Fig. 2). These critical values are in very good agreement with earlier studies investigating the bulk system, where a transition to the unstable regime was found at a doping concentration of $c_{Nb} = 0.8\%$ [26]. Thus, a stable polaron in STO is linked to a critical concentration of defects (or other polarons) in its vicinity. Our data do not suggest a sizable overlap between a polaron and its periodic image, ruling out polaron-polaron interaction as the driving force for the stabilization of a small polaron, which is rather due to the interaction with the Nb defect, as previously elaborated. An appreciable overlap between polaron charges in neighboring supercells is observed only for the higher doping level ($1/N_{unitcell} = 0.25$),
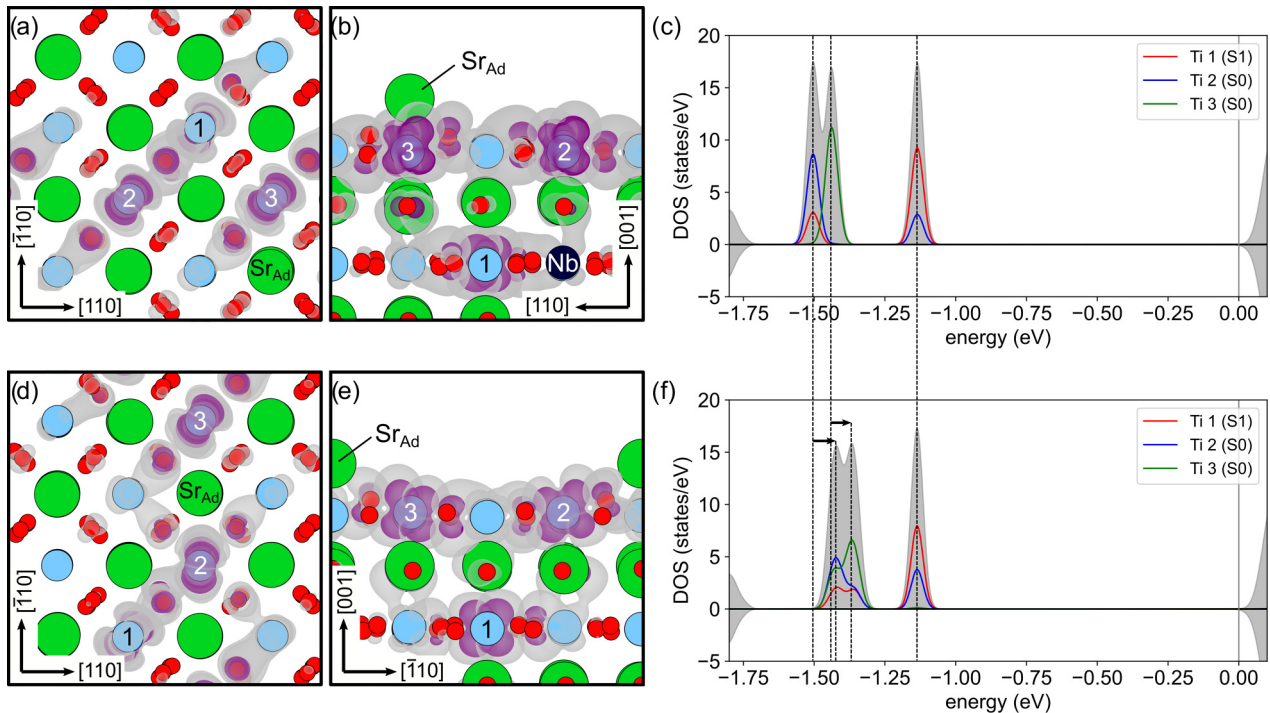
FIG. 4. (a) Top and (b) side views of the lowest-energy polaron configuration for the experimental slab. Two polarons are localized in the S0 layer, and the third one is localized in the S1 layer. (c) PDOS plot for the lowest-energy polaron configuration; surface polarons (Ti 2 and 3) appear as distinct peaks and are lower in energy than the subsurface polaron peak (Ti 1). (d) Top and (e) side views for a different three-polaron configuration. This configuration is higher in energy due to one surface polaron (Ti 2) now being localized farther away from Nb, as well as unfavorable polaron orbital rotations. (f) Corresponding PDOS, where polaron peaks of the surface polarons (Ti 2 and 3) are shifted higher up in energy compared to the lowest-energy configuration. The PDOS shows a strong charge sharing between polaronic sites, resulting in the formation of a multipolaron complex.

but the corresponding polaron formation energy is higher than the one expected from the linear decrease.

The change in polaron stability can be attributed to a twofold effect: (1) a reduced flexibility of the lattice at lower doping concentrations, as already suggested for the bulk system [26], and (2) an electronic effect, in which the Nb doping atom creates a stabilizing positive potential in its vicinity. Both these contributions lead to increased polaron stability in doping-rich environments (see also Fig. SF5 in [51]).

B. The as-cleaved TiO₂ termination

We modeled the as-cleaved TiO_2 termination considering two different setups: (1) an undoped $2\sqrt{2} \times 2\sqrt{2} \times 6$ slab with one Sr adatom adsorbed, leading to two small electron polarons in the supercell, and (2) an Nb-doped slab of the same size together with the adsorbed Sr adatom, resulting in three excess charge carriers total.

For the first case, only the Sr adatom acts as an electron donor, and the lowest-energy configuration is represented by two small polarons localizing at S0 Ti atoms (see Fig. 3). This appears to be a reasonable solution, considering that S0 polarons are more stable than S1 polarons, as shown in Fig. 2(e) for the bulklike termination. Further, with only two polarons occupying the same layer, there is enough space to prevent strong repulsion between them. The charge of the two polarons is aligned in parallel directions, as shown in

Figs. 3(a) and 3(b): This orientation shows minimal overlap of the polaronic charge densities, minimizing the repulsive interaction.

The polaron localized at the Ti atom next to the Sr adatom shows a slightly lower formation energy, as indicated by the two in-gap polaron peaks in the density of states in Fig. 3(c). The expected pattern would be localizing both (negatively charged) polarons near the (positively charged) Sr adatom, at Ti atoms on opposite sides of the adatom. However, this configuration is disfavored by 38 meV, possibly due to the polaronic charge of one polaron spreading towards the adatom, creating a repulsive environment for the other (as evident also from the simulated STM images reported in Sec. III C). All other available S0 Ti sites show very similar formation energy for the localization of the second polaron.

In the Nb-doped slab, the scenario becomes more complicated due to the higher number of charge carriers (one induced by the Nb, two induced by the Sr adatom). As discussed for bulklike termination, the Nb atom creates an energy minimum for polaron localization at its nearest-neighbor Ti atoms in both the S1 and S0 layers. The lowest-energy configuration for the Nb-doped slab with the Sr adatom is retrieved by localizing two polarons in the S0 layer, one directly on top of the Nb atom and the other at a Ti site next to the Sr adatom, and localizing one polaron at a Ti site next to Nb in the S1 layer [see Figs. 4(a) and 4(b)]. The corresponding density of states is shown in Fig. 4(c). The S1 polaron peak is clearly
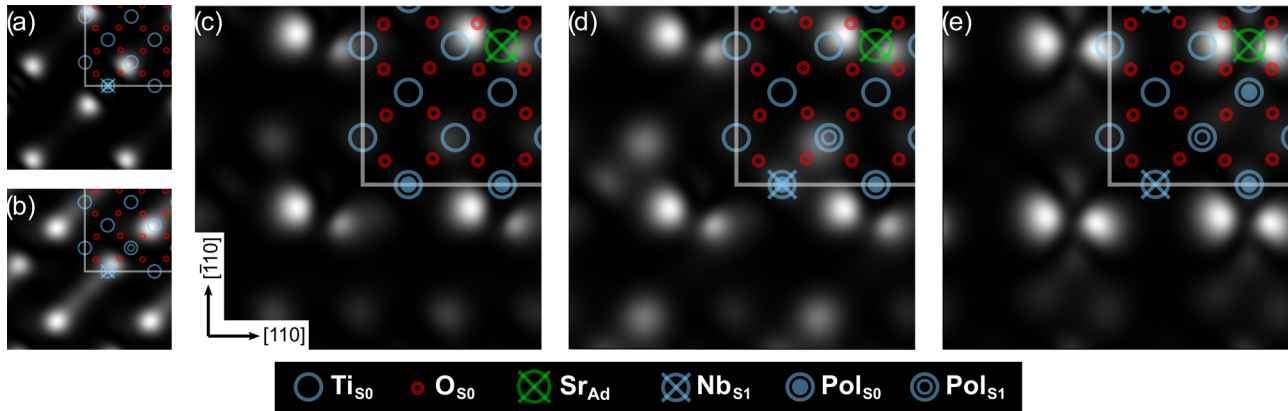
FIG. 5. Simulated STM images taken 3 Å above the surface of the $2\sqrt{2} \times 2\sqrt{2} \times 6$ cell. The image is replicated in lateral directions for better visualization of the features. A single supercell is indicated by the overlay, in which different defects and polaron positions are marked. For overlapping features at the same lattice position, the respective markers are superimposed. (a) System with one polaron localized in the S0 layer, directly on top of the Nb doping. (b) One polaron localized at a Ti atom next to the Nb doping within the S1 layer. (c) Two polarons localized in the S0 layer, introduced by the Sr adatom. (d) Lowest-energy configuration for three polarons with both defects present in the supercell, Nb doping and the Sr adatom. One polaron is localized in the S1 layer next to the Nb atom, and two are localized in the S0 layer. (e) Another configuration with three polarons for which charge sharing between different polaronic sites is especially pronounced [see Fig. 4(f)].

higher in energy, in line with a less favorable E_{pol}, as discussed for the bulklike termination. The degeneracy in energy for the two S0 polarons is lifted due to the defects, where the lower-energy peak is associated with the S0 polaron being directly above Nb. Due to the large density of carriers, the polaronic states can get affected by a sizable overlap of the charge densities: The density of states (DOS) clearly shows that the S1 polaron spreads over the Ti site hosting one of the two S0 polarons (see the red and blue peaks in the DOS).

For comparison, Figs. 4(d) and 4(e) show a different polaron configuration, characterized by a less stable total formation energy, $\Delta E_{pol} = +124$ meV. The corresponding in-gap DOS [Fig. 4(f)] reveals a similar electronic structure, with the polaronic peaks shifted towards higher energy, in line with the less favorable E_{pol}. This might arise from increased polaron-polaron repulsion due to the enhanced overlap of the polaronic orbitals (see the smeared peaks in the DOS), as well as a less favorable orientation of polaron orbitals.

C. Simulated STM

The SSTM pictures of all previously discussed polaron systems are collected in Fig. 5. Single-polaron systems with one polaron in S0 and S1 are shown in Figs. 5(a) and 5(b), respectively. These are the systems discussed in Sec. III A using a Nb-doped slab with bulklike termination. For both S0 and S1 polarons, a double-dot signal is observed for each single polaron. The strongest signal originates from charge localized at Ti-O bonds at the surface but not directly adjacent to the localization site. The bond lobes creating this signal are marked in Fig. 2(b).

Figure 5(c) depicts the SSTM image of the undoped slab, with only the Sr adatom present as an electron donor. Both polarons are localized in S0, as shown in Fig. 3, and again, the strongest signal is located at surface Ti-O bonds. Furthermore, charge is accumulated around the Sr adatom.

The lowest-energy configuration for the as-cleaved slab with a Sr adatom and Nb doping is shown in Fig. 5(d). This surface slab recreates the experimental surface the most accurately of all systems investigated here. The SSTM picture looks very similar to the undoped slab in Fig. 5(c), with S0 polaron charge accumulating around the Sr adatom. However, there is also a stronger signal visible at a Ti-O bond farther away from the adatom, caused by the additional S1 polaron.

A SSTM picture of the alternative polaronic configuration depicted in Figs. 4(d) and 4(e) is shown in Fig. 5(e). This system has enhanced charge accumulation around the Sr adatom, resulting in a stronger and more symmetric feature in the SSTM signal. The S1 polaron signal is suppressed, and the charge is most likely incorporated in the strong signal around the adatom. This shows that multiple polarons close to each other may lead to very different patterns in SSTM, in which charge spreading between polaronic sites can suppress or enhance certain features in the picture.

Summarizing, from the generated SSTM images two main findings can be deducted: (1) An isolated, double-lobed signal in STM images likely corresponds to a single polaron, and (2) the polaronic charge tends to accumulate around the surface defects. These SSTM results could be beneficial in the interpretation of future STM measurements, as they provide clear references to the electronic hallmarks of surface charge carriers.

IV. CONCLUSIONS

In the presented work we modeled polaron formation on an unreconstructed STO(001) surface with TiO$_2$ termination while taking into account chemical doping and defects. Our thorough classification of polarons hosted in this system leads to several relevant findings, all of which could help unravel the specific roles of these quasiparticles in STO in future theoretical and experimental research.

First, we were able to extend a known trend for STO bulk systems, that polarons tend to be more stable in doping-rich environments, to the STO(001) surface. Consequently, when moving towards the dilute limit, e.g., low doping concentra-

tion, polarons are progressively destabilized until they become unstable for sparse doping environments. For polarons localized in the subsurface (S1) TiO_2 layer this crossover occurs at roughly the same doping concentration as for bulk systems [26], while polarons at the surface (S0) are more stable. This result provides further support for the claimed competition between small polarons and delocalized charge states, e.g., in form of large polarons or 2DEG in this system, or the possible coexistence of such localized and delocalized charge in different regions of the crystal. A thorough classification of the less localized charge or large polarons in the system, however, would require a different methodology as employed here [54–56].

Next, we modeled the recently obtained, as-cleaved STO(001) surface with a TiO_2 termination, a prime example of a flat (001) perovskite oxide surface. This was achieved by considering Sr adatoms and Nb doping simultaneously in the same simulated slab. Using realistic defect and doping concentrations, our data suggest that under these conditions the STO system hosts three polarons per supercell. The resulting polaron patterns are rationalized by several overlapping effects: On the one hand, the negatively charged small electron polarons energetically favor a separation between each other due to repulsive polaron-polaron interactions; on the other hand, they are attracted to the positively charged defects, in this case the positively charged Nb and Sr ions. The resulting configuration is formed by two polarons localized in the S0 layer and the third polaron being pushed down to the S1 layer. Further, polarons localized directly on the surface in the S0 layer are more stable and energetically preferred, suggesting that they can more easily interact with external adsorbates.

An additional mechanism that influences the stability of the studied multipolaron system is polaron charge spreading over several different polaronic Ti sites, as well as polaron orbital ordering, which leads to rotations and reorientations of polaron lobes with respect to each other [57]. In a very hybridized configuration, one polaron orbital rotates out of the typical lowest-energy position, no longer aligning its orbital lobes with the surrounding TiO_6 octahedra. Charge sharing or polaron clustering may be a way to increase polaron stability in a densely populated environment.

The spectroscopic signal of polarons was analyzed by means of SSTM images. A single polaron, localized in either the S0 or S1 layer, creates a distinct, double-dot signal (rather than a single feature), while more complex patterns emerge in environments hosting multiple polarons. Polaronic charge is found primarily in Ti-O bonds at the surface and accumulated around the surface defects, when present. This charge accumulation could lead to altering adatom appearances in experimental images. Charge spreading between polaronic sites can lead to the suppression or enhancement of certain features in the STM picture, further complicating the interpretation.

Overall, our study provides additional theoretical evidence for the polaronic behavior of STO(001) and helps interpret the growing amount of experimental data measured on its pristine and unreconstructed terminations. Future work will follow this analysis. Possible directions involve exploring polaron transport, multipolaron interactions, and the possible formation of bipolarons [58,59]. Another natural continuation would be the investigation of more complex scenarios, specifically, the interaction between polarons and adsorbates, as well as the possible coexistence of small electron and hole polarons as self-trapped excitons, two aspects key to designing energy applications based on STO.

ACKNOWLEDGMENTS

[1] A. F. Santander-Syro, O. Copie, T. Kondo, F. Fortuna, S. Pailhès, R. Weht, X. G. Qiu, F. Bertran, A. Nicolaou, A. Taleb-Ibrahimi, P. Le Fèvre, G. Herranz, M. Bibes, N. Reyren, Y. Apertet, P. Lecoeur, A. Barthélémy, and M. J. Rozenberg, Two-dimensional electron gas with universal subbands at the surface of SrTiO₃, Nature (London) **469**, 189 (2011).

[2] Z. Wang, Z. Zhong, X. Hao, S. Gerhold, B. Stoger, M. Schmid, J. Sanchez-Barriga, A. Varykhalov, C. Franchini, K. Held, and U. Diebold, Anisotropic two-dimensional electron gas at SrTiO₃(110), Proc. Natl. Acad. Sci. USA **111**, 3933 (2014).

[3] C. Li, Z. Liu, W. Lü, X. R. Wang, A. Annadi, Z. Huang, S. Zeng, Ariando, and T. Venkatesan, Tailoring the two dimensional electron gas at polar ABO₃/SrTiO₃ interfaces for oxide electronics, Sci. Rep. **5**, 13314 (2015).

[4] D. Kan, T. Terashima, R. Kanda, A. Masuno, K. Tanaka, S. Chu, H. Kan, A. Ishizumi, Y. Kanemitsu, Y. Shimakawa, and M. Takano, Blue-light emission at room temperature from Ar⁺-irradiated SrTiO₃, Nat. Mater. **4**, 816 (2005).

[5] Y. Liu, L. Xie, Y. Li, R. Yang, J. Qu, Y. Li, and X. Li, Synthesis and high photocatalytic hydrogen production of SrTiO₃ nanoparticles from water splitting under UV irradiation, J. Power Sources **183**, 701 (2008).

[6] X. Guan and L. Guo, Cocatalytic effect of SrTiO₃ on Ag₃PO₄ toward enhanced photocatalytic water oxidation, ACS Catal. **4**, 3020 (2014).

[7] S. Shoji, G. Yin, M. Nishikawa, D. Atarashi, E. Sakai, and M. Miyauchi, Photocatalytic reduction of CO₂ by CuₓO nanocluster loaded SrTiO₃ nanorod thin film, Chem. Phys. Lett. **658**, 309 (2016).

[8] H. Ouhbi and J. Wiktor, Polaron formation and hopping in tantalate perovskite oxides: $NaTaO_3$ and $KTaO_3$, Phys. Rev. B **104**, 235158 (2021).

[9] N. Reyren, S. Thiel, A. D. Caviglia, L. F. Kourkoutis, G. Hammerl, C. Richter, C. W. Schneider, T. Kopp, A.-S. Rueetschi, D. Jaccard, M. Gabay, D. A. Muller, J.-M. Triscone, and J. Mannhart, Superconducting interfaces between insulating oxides, Science **317**, 1196 (2007).

[10] H. Lim, C. Song, M. Seo, D. Kim, M. Jung, H. Kang, S. Kim, K.-J. Lee, Y. Yu, G. Kim, K.-J. Kim, and B. S. Mun, Nature of the surface space charge layer on undoped $SrTiO_3$ (001), J. Mater. Chem. C **9**, 13094 (2021).

[11] E. Bonini Guedes, T. Willemoes Jensen, M. Naamneh, A. Chikina, R. T. Dahm, S. Yun, F. M. Chiabrera, N. C. Plumb, J. H. Dil, M. Shi, D. Valbjørn Christensen, W. Hugo Brito, N. Pryds, and M. Radović, Disclosing the response of the surface electronic structure in $SrTiO_3$ (001) to strain, J. Vac. Sci. Technol. A **40**, 013213 (2022).

[12] J. Goniakowski and C. Noguera, The concept of weak polarity: An application to the $SrTiO_3$(001) surface, Surf. Sci. **365**, L657 (1996).

[13] C. Noguera, Polar oxide surfaces, J. Phys.: Condens. Matter **12**, R367 (2000).

[14] A. Sahoo, D. Nafday, T. Paul, R. Ruiter, A. Roy, M. Mostovoy, T. Banerjee, T. Saha-Dasgupta, and A. Ghosh, Out-of-plane interface dipoles and anti-hysteresis in graphene-strontium titanate hybrid transistor, npj 2D Mater. Appl. **2**, 9 (2018).

[15] J. A. Enterkin, A. K. Subramanian, B. C. Russell, M. R. Castell, K. R. Poeppelmeier, and L. D. Marks, A homologous series of structures on the surface of $SrTiO_3$(110), Nat. Mater. **9**, 245 (2010).

[16] I. Sokolović, G. Franceschi, Z. Wang, J. Xu, J. Pavelec, M. Riva, M. Schmid, U. Diebold, and M. Setvín, Quest for a pristine unreconstructed $SrTiO_3$(001) surface: An atomically resolved study via noncontact atomic force microscopy, Phys. Rev. B **103**, L241406 (2021).

[17] I. Sokolović, M. Schmid, U. Diebold, and M. Setvin, Incipient ferroelectricity: A route towards bulk-terminated $SrTiO_3$, Phys. Rev. Mater. **3**, 034407 (2019).

[18] L. D. Landau, Über die Bewegung der Elektronen in Kristallgitter, Phys. Z. Sowjetunion **3**, 644 (1933).

[19] C. Franchini, M. Reticcioli, M. Setvin, and U. Diebold, Polarons in materials, Nat. Rev. Mater. **6**, 560 (2021).

[20] C. Spreafico and J. VandeVondele, The nature of excess electrons in anatase and rutile from hybrid DFT and RPA, Phys. Chem. Chem. Phys. **16**, 26144 (2014).

[21] A. J. E. Rettie, W. D. Chemelewski, D. Emin, and C. B. Mullins, Unravelling small-polaron transport in metal oxide photoelectrodes, J. Phys. Chem. Lett. **7**, 471 (2016).

[22] D. Zhang, Z. K. Han, G. E. Murgida, M. V. Ganduglia-Pirovano, and Y. Gao, Oxygen-Vacancy Dynamics and Entanglement with Polaron Hopping at the Reduced CeO_2(111) Surface, Phys. Rev. Lett. **122**, 096101 (2019).

[23] G. H. Jaffari, M. Akram, L. Zia, A. Ali, and Q. ul Hassan, Acceptor-donor concentration dependent polaronic relaxation, pinned electron defect dipole characteristic and colossal permittivity in co-doped rutile $(Zn_{1/3}Nb_{2/3})_xTi_{1-x}O_2$ ($x = 0.02$, 0.04, 0.06 and 0.08) ceramics, Phys. B (Amsterdam, Neth) **640**, 414082 (2022).

[24] Z. He, M. Cao, E. Furman, M. T. Lanagan, M. Yuan, X. Meng, J. Wu, H. Hao, Z. Yao, Z. Yu, and H. Liu, Anomalous dielectric relaxation peak in Nb-doped $SrTiO_3$ single crystals, Ceramics Int. **48**, 24725 (2022).

[25] M. Crespillo, J. Graham, F. Agulló-López, Y. Zhang, and W. Weber, Isolated oxygen vacancies in strontium titanate shine red: Optical identification of Ti^{3+} polarons, Appl. Mater. Today **12**, 131 (2018).

[26] X. Hao, Z. Wang, M. Schmid, U. Diebold, and C. Franchini, Coexistence of trapped and free excess electrons in $SrTiO_3$, Phys. Rev. B **91**, 085204 (2015).

[27] H. O. Jeschke, J. Shen, and R. Valentí, Localized versus itinerant states created by multiple oxygen vacancies in $SrTiO_3$, New J. Phys. **17**, 023034 (2015).

[28] A. Janotti, J. B. Varley, M. Choi, and C. G. Van de Walle, Vacancies and small polarons in $SrTiO_3$, Phys. Rev. B **90**, 085202 (2014).

[29] S. Dadgostar, J. L. Pura Ruiz, J. Serrano Gutierrez, B. Lepine, P. Schieffer, and J. Jimenez, Luminescence in undoped and Nb-doped $SrTiO_3$ crystals: Bulk and surface emission, Mater. Sci. Eng. B **283**, 115830 (2022).

[30] Z. He, M. Cao, Y. Tao, X. Meng, J. Wu, H. Hao, Z. Yao, Z. Yu, H. Liu, E. Furman, and M. T. Lanagan, Giant permittivity in Nb-doped $SrTiO_3$ single crystal: Compositional gradient and local structure, Ceram. Int. **48**, 29572 (2022).

[31] R. I. Eglitis, *Ab initio* calculations of $SrTiO_3$, $BaTiO_3$, $PbTiO_3$, $CaTiO_3$, $SrZrO_3$, $PbZrO_3$ and $BaZrO_3$ (001), (011) and (111) surfaces as well as F centers, polarons, KTN solid solutions and Nb impurities therein, Int. J. Mod. Phys. B **28**, 1430009 (2014).

[32] C. Ricca, I. Timrov, M. Cococcioni, N. Marzari, and U. Aschauer, Self-consistent DFT $+ U + V$ study of oxygen vacancies in $SrTiO_3$, Phys. Rev. Res. **2**, 023313 (2020).

[33] J. Souto-Casares, N. A. Spaldin, and C. Ederer, Oxygen vacancies in strontium titanate: A DFT + DMFT study, Phys. Rev. Res. **3**, 023027 (2021).

[34] C. Cheng and R. Long, Charge-compensated doping extends carrier lifetimes in $SrTiO_3$ by passivating oxygen vacancy defects, J. Phys. Chem. Lett. **12**, 12040 (2021).

[35] J. T. Devreese, S. N. Klimin, J. L. M. van Mechelen, and D. van der Marel, Many-body large polaron optical conductivity in $SrTi_{1-x}Nb_xO_3$, Phys. Rev. B **81**, 125119 (2010).

[36] S. Klimin, J. Tempere, J. T. Devreese, C. Franchini, and G. Kresse, Optical response of an interacting polaron gas in strongly polar crystals, Appl. Sci. **10**, 2059 (2020).

[37] C. Verdi, F. Caruso, and F. Giustino, Origin of the crossover from polarons to Fermi liquids in transition metal oxides, Nat. Commun. **8**, 15769 (2017).

[38] J. L. M. van Mechelen, D. van der Marel, C. Grimaldi, A. B. Kuzmenko, N. P. Armitage, N. Reyren, H. Hagemann, and I. I. Mazin, Electron-Phonon Interaction and Charge Carrier Mass Enhancement in $SrTiO_3$, Phys. Rev. Lett. **100**, 226403 (2008).

[39] G. Kresse and J. Hafner, *Ab initio* molecular dynamics for open-shell transition metals, Phys. Rev. B **48**, 13115 (1993).

[40] G. Kresse and J. Furthmüller, Efficiency of *ab-initio* total energy calculations for metals and semiconductors using a plane-wave basis set, Comput. Mater. Sci. **6**, 15 (1996).

[41] G. Kresse and J. Furthmüller, Efficient iterative schemes for ab initio total-energy calculations using a plane-wave basis set, Phys. Rev. B **54**, 11169 (1996).

[42] P. E. Blöchl, Projector augmented-wave method, Phys. Rev. B **50**, 17953 (1994).

[43] J. P. Perdew, K. Burke, and M. Ernzerhof, Generalized Gradient Approximation Made Simple, Phys. Rev. Lett. **77**, 3865 (1996).

[44] G. Kresse and D. Joubert, From ultrasoft pseudopotentials to the projector augmented-wave method, Phys. Rev. B **59**, 1758 (1999).

[45] S. L. Dudarev, G. A. Botton, S. Y. Savrasov, C. J. Humphreys, and A. P. Sutton, Electron-energy-loss spectra and the structural stability of nickel oxide: An LSDA+U study, Phys. Rev. B **57**, 1505 (1998).

[46] Z. Hou and K. Terakura, Defect states induced by oxygen vacancies in cubic $SrTiO_3$: First-principles calculations, J. Phys. Soc. Jpn. **79**, 114704 (2010).

[47] M. Choi, F. Oba, Y. Kumagai, and I. Tanaka, Antiferrodistortive-like oxygen-octahedron rotation induced by the oxygen vacancy in cubic $SrTiO_3$, Adv. Mater. **25**, 86 (2013).

[48] T. Yamanaka, N. Hirai, and Y. Komatsu, Structure change of $Ca_{1-x}Sr_xTiO_3$ perovskite with composition and pressure, Am. Mineral. **87**, 1183 (2002).

[49] G. Makov and M. C. Payne, Periodic boundary conditions in *ab initio* calculations, Phys. Rev. B **51**, 4014 (1995).

[50] J. Neugebauer and M. Scheffler, Adsorbate-substrate and adsorbate-adsorbate interactions of Na and K adlayers on Al(111), Phys. Rev. B **46**, 16067 (1992).

[51] See Supplemental Material at http://link.aps.org/supplemental/10.1103/PhysRevMaterials.7.064602 for additional details concerning the study design and polaron formation energies.

[52] M. Reticcioli, U. Diebold, G. Kresse, and C. Franchini, Small polarons in transition metal oxides, in *Handbook of Materials Modeling*, edited by W. Andreoni, and S. Yip (Springer, Cham, Switzerland, 2019), pp. 1–39.

[53] J. P. Allen and G. W. Watson, Occupation matrix control of *d*- and *f*-electron localisations using DFT + *U*, Phys. Chem. Chem. Phys. **16**, 21016 (2014).

[54] W. H. Sio, C. Verdi, S. Poncé, and F. Giustino, Polarons from First Principles, without Supercells, Phys. Rev. Lett. **122**, 246403 (2019).

[55] W. H. Sio, C. Verdi, S. Poncé, and F. Giustino, *Ab initio* theory of polarons: Formalism and applications, Phys. Rev. B **99**, 235139 (2019).

[56] J. Lafuente-Bartolome, C. Lian, W. H. Sio, I. G. Gurtubay, A. Eiguren, and F. Giustino, *Ab initio* self-consistent many-body theory of polarons at all couplings, Phys. Rev. B **106**, 075119 (2022).

[57] M. Reticcioli, M. Setvin, M. Schmid, U. Diebold, and C. Franchini, Formation and dynamics of small polarons on the rutile $TiO_2(110)$ surface, Phys. Rev. B **98**, 045306 (2018).

[58] M. Capone, M. Grilli, and W. Stephan, Small polaron formation in many-particle states of the Hubbard-Holstein model: The one-dimensional case, Eur. Phys. J. B **11**, 551 (1999).

[59] J. Krsnik, I. Batistić, A. Marunović, E. Tutiš, and O. S. Barišić, Exact solution of electronic transport in semiconductors dominated by scattering on polaronic impurities, Phys. Rev. B **102**, 241111(R) (2020).